

Photochemical mechanism of DEACM uncaging: A combined time-resolved spectroscopic and computational study

C. Hamerla¹, C. Neumann², K. Falahati¹, J. von Cosel¹, L. J. G. W. van Wilderen², M. S. Niraghatam¹, D. Kern-Michler², N. Mielke², M. Reinfelds³, A. Rodrigues-Correia³, A. Heckel³, J. Bredenbeck^{*2}, and I. Burghardt^{*1}

¹*Institute of Physical and Theoretical Chemistry, Goethe University Frankfurt, Max-von-Laue-Str. 7, 60438 Frankfurt/Main, Germany*

²*Institute of Biophysics, Goethe University Frankfurt, Max-von-Laue-Str. 1, 60438 Frankfurt/Main, Germany*

³*Institute for Organic Chemistry and Chemical Biology, Goethe University Frankfurt, Max-von-Laue-Str. 9, 60438 Frankfurt am Main, Germany*

Contents

S1 Sample preparation and characterization	3
S1.1 DEACM-SCN	3
S1.2 DEACM-Carb	4
S2 Steady-state absorption experiments	6
S2.1 UV/Vis spectra	6
S2.2 FTIR spectra	8
S3 Ultrafast pump-probe experiments	9
S3.1 ESA and product formation kinetics of all acetonitrile/water mixtures . . .	9
S3.2 Raw data and global analysis of 95%/5% acetonitrile/water mixture . . .	11
S3.3 Raw data and global analysis of 50%/50% acetonitrile/water mixture . . .	13
S4 Computational analysis	15
S4.1 Optimized structures of the DEACM species	15
S4.2 Ground-state equilibrium structures: dihedral angle α_{CCCX}	20
S4.3 Constraints for relaxed surface scans	23

S4.4 Vertical excitations	24
S4.5 Geometry optimization in the S_1 state	26
S4.6 Solvent effects on excited states	28
S4.7 Effect of LR-PCM vs. state-specific (SS-PCM) solvation	31
S4.8 Charge analysis as a function of R_{C-X} distance	34
S4.9 State crossings of low-lying singlet states with dissociative states	38

S1 Sample preparation and characterization

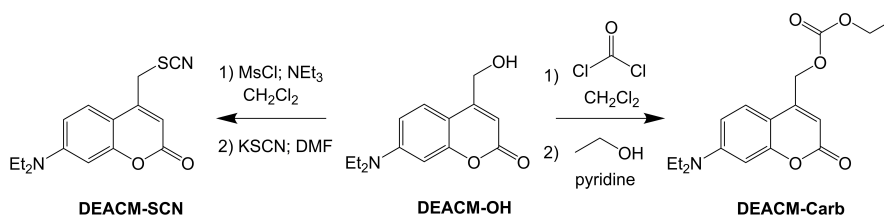


Figure S1: Synthesis of DEACM-SCN and DEACM-Carb.

All solvents and reagents were purchased from commercial sources and used without further purification. TLC was performed using Macherey-Nagel precoated TLC-sheets ALUGRAM Xtra SIL G/UV254 and visualization was done under UV light (254 and 365 nm). For column chromatography a Machery-Nagel silica gel 60 (particle size 0.04-0.06 mm) was used. NMR spectra were measured on a Bruker AV 500 or AV 400 MHz device, using CDCl₃ as solvent. The spectra were referenced to the residual CHCl₃ peak (¹H 7.26 ppm, ¹³C 77.16 ppm). Chemical shifts (δ) are reported on a ppm scale. Following abbreviations (or combinations thereof) were used to describe multiplicities: s = singlet, d = doublet, t = triplet, q = quartet. Coupling constants (J) are reported in Hertz (Hz). Mass spectrometry was performed on ThermoFisher Surveyor MSQTM (ESI - Electrospray ionization) and MALDI-LTQ Orbitrap XLTM (HRMS - High-Resolution Mass Spectrometry) device from Thermo Fisher Scientific.

S1.1 DEACM-SCN

The synthesis of DEACM-SCN was carried out analogously to the previously described procedure for the synthesis of DEACM-N₃ (see Ref. 21). DEACM-OH (725 mg, 2.9 mmol, 1 eq) was dissolved in dry CH₂Cl₂ (10 mL) and mixed with Et₃N (594 mg, 5.8 mmol, 2 eq). The solution was cooled in an ice bath before dropwise addition of methanesulfonyl chloride (504 mg, 4.4 mmol, 1.5 eq). After stirring for 1.5 h the mixture was diluted with CH₂Cl₂, washed with saturated NaHCO₃ solution and brine, dried over Na₂SO₄ and concentrated under reduced pressure to yield the mesylated product. The crude mesylated coumarin (362 mg, 1.4 mmol) was dissolved in dry DMF (7 mL) and KSCN (568 mg, 5.8 mmol, 4.1 eq) was added. The mixture was stirred overnight at room temperature. Upon completion the mixture was diluted with EtOAc, extracted with half-saturated NaCl solution (3 x 30 mL), washed with brine, dried over Na₂SO₄ and concentrated under reduced pressure. The product was purified by a column chromatography (SiO₂, cyclohexane : ethylacetate 3:1) to yield 368 mg (87%) of orange powder. ¹H NMR (500 MHz, CDCl₃): δ 7.32 (d, 1H, J = 9.0 Hz), 6.61 (dd, 1H, J = 9.0, 2.6 Hz), 6.53 (d, 1H, J = 2.6 Hz), 6.12 (s, 1H), 4.15 (s, 2H), 3.43 (q, 4H, J = 7.1 Hz), 1.22 (t, 6H, J = 7.1 Hz) ppm. ¹³C NMR (125 MHz, CDCl₃): δ 161.1, 156.9, 151.2, 147.4, 124.8, 110.7, 110.2, 108.9, 105.8, 98.3, 45.0, 33.9, 12.6 ppm. HRMS (MALDI) m/z: [M+H]⁺ Calc. for C₁₅H₁₇N₂O₂S 289.10053; Found 289.10054.

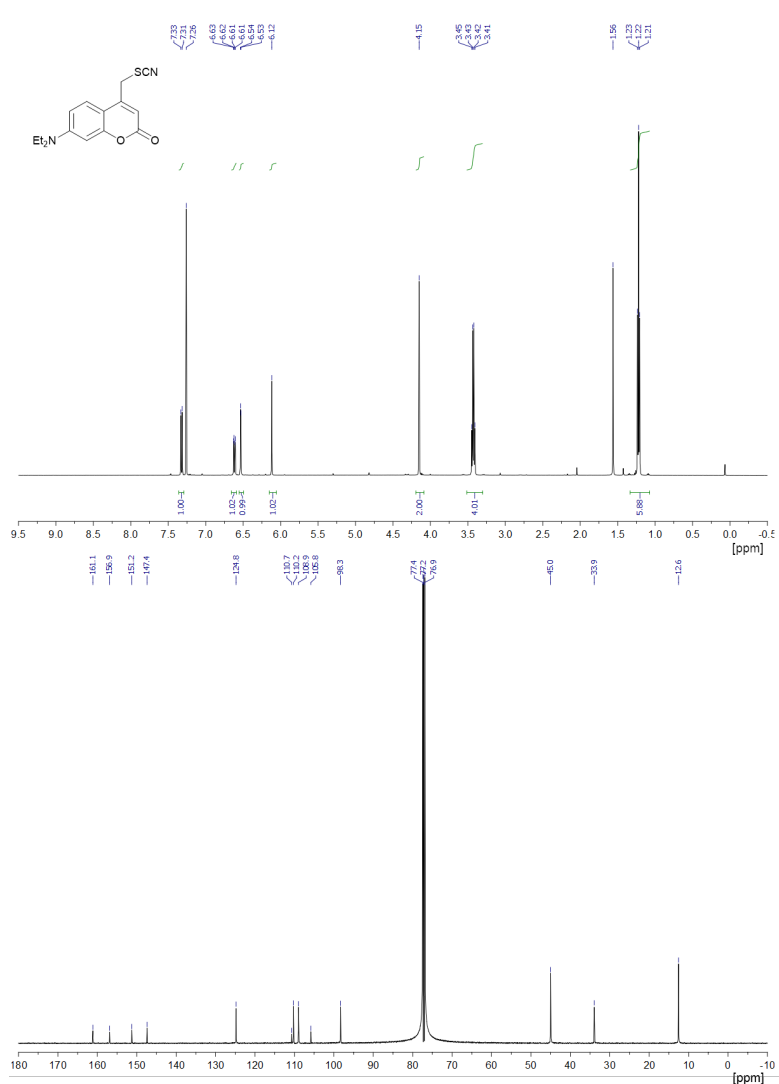


Figure S2: ¹H (500 MHz, upper) and ¹³C {*H*} (125 MHz, lower) NMR spectra of DEACM-SCN in CDCl₃.

S1.2 DEACM-Carb

Phosgene (~20% in toluene, 6.3 mL, 12.0 mmol, 5 eq; **phosgene is a poison, work exclusively in fume hood**) was mixed with 15 mL of a dry CH₂Cl₂ and cooled in an ice bath. DEACM-OH (590 mg, 2.4 mmol, 1 eq) was dissolved in dry CH₂Cl₂ and dropwise added to the phosgene solution. The resulting mixture was stirred at a room temperature for 3h, then the leftover phosgene was removed by a gentle stream of argon (**in fume hood!**). Ethanol (10 mL) and pyridine (0.19 mL, 2.4 mmol, 1 eq) was added and the mixture stirred overnight. Upon completion the solvent was removed, and the crude product purified by a column chromatography (SiO₂, CH₂Cl₂ : acetone 50:1) to

yield 170 mg (22%) of brown powder. ^1H NMR (400 MHz, CDCl_3): δ 7.28 (d, 1H, $J = 9.0$ Hz), 6.58 (dd, 1H, $J = 9.0, 2.5$ Hz), 6.51 (d, 1H, $J = 2.5$ Hz), 6.15 (t, 1H, $J = 1.1$ Hz), 5.25 (d, 2H, $J = 1.1$ Hz), 4.25 (q, 2H, $J = 7.1$ Hz), 3.40 (q, 4H, $J = 7.1$ Hz), 1.34 (t, 3H, $J = 7.2$ Hz), 1.20 (t, 6H, $J = 7.1$ Hz) ppm. ^{13}C NMR (100 MHz, CDCl_3): δ 161.7, 156.3, 154.7, 150.5, 148.8, 124.4, 108.9, 106.8, 106.1, 98.1, 64.8, 64.4, 44.9, 14.2, 12.4 ppm. ESI-MS, m/z : $[\text{M}+\text{H}]$ 320.0 (100)

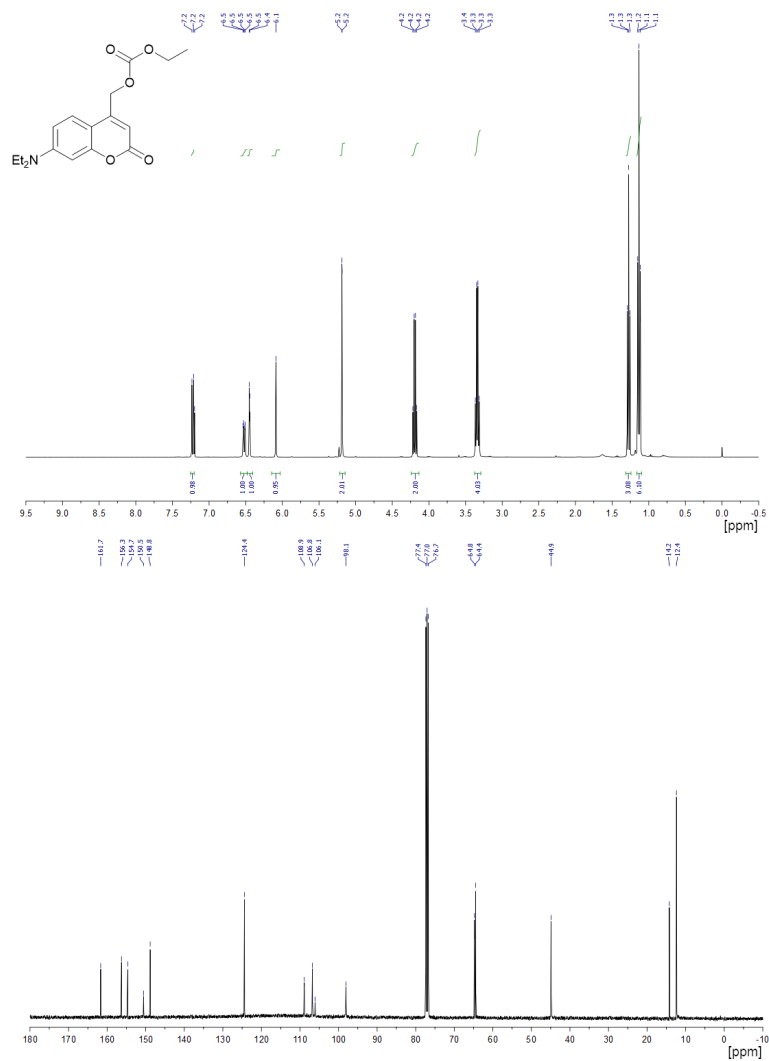


Figure S3: ^1H (500 MHz, upper) and ^{13}C $\{^1\text{H}\}$ (100 MHz, lower) NMR spectra of DEACM-Carb in CDCl_3 .

S2 Steady-state absorption experiments

S2.1 UV/Vis spectra

The photocages were not only measured in pure acetonitrile but also in mixtures of acetonitrile and 5 vol-% and 50 vol-% of D₂O in order to study the influence of water (which is the solvent relevant for biological applications of the DEACM photocage) on the uncaging reaction. As H₂O obscured the spectral region between 1600 cm⁻¹ and 1700 cm⁻¹ where two relevant ring modes were found to absorb, D₂O was used instead of H₂O. In order to allow for a clear presentation of the effect the leaving group has on the uncaging kinetics and to facilitate the comparison of the three different species, the main paper only presents the data measured in pure acetonitrile. Here, also the spectra acetonitrile/D₂O mixtures are shown.

As seen in Figure S4, the spectral shape of all three compounds is almost identical with one broad absorption maximum below 400 nm. Whereas DEACM-N₃ and DEACM-Carb exhibit quite similar central wavelengths (at 377.5 nm and 378 nm, respectively), the absorption spectrum of DEACM-SCN is slightly red-shifted and has its absorption maximum at 389.5 nm. With addition of D₂O the absorption maximum was found to shift red by a few nm (see Fig. S5).

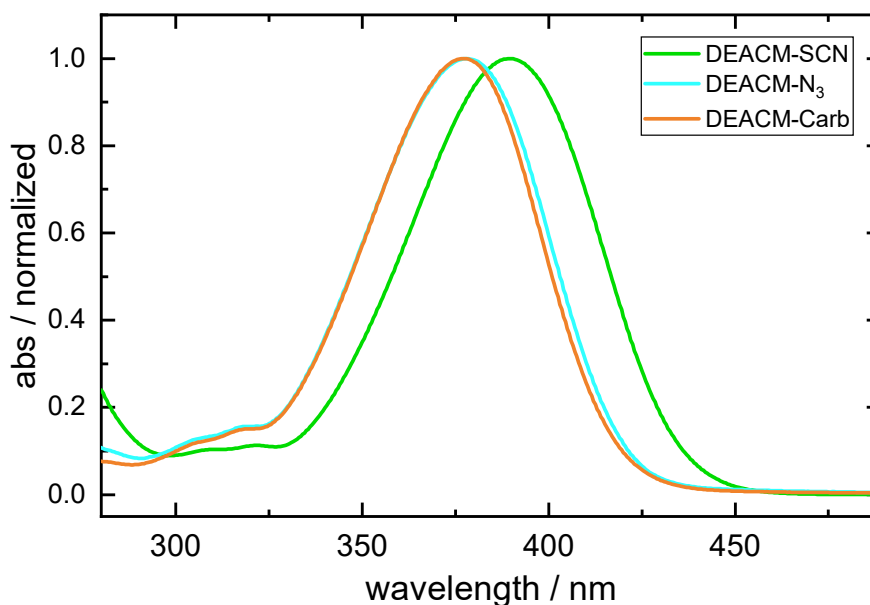


Figure S4: Steady state UV/Vis absorption spectra of DEACM-SCN (green), DEACM-N₃ (blue; adapted from Ref. 21 with permission from The Royal Society of Chemistry) and DEACM-Carb (orange). The spectra were measured at a concentration of 0.25 mM in a cuvette with an optical path length of 1 mm. The solvent spectrum was subtracted and the obtained data were normalized to the absorption maximum to facilitate an easy comparison of the different compounds.

The addition of water slightly modulates the absorption bands as shown in Figure S5 (left column). The light-induced difference spectra all show a clear red-shifted product, regardless of the water content (shown in the right column for all solvent mixtures).

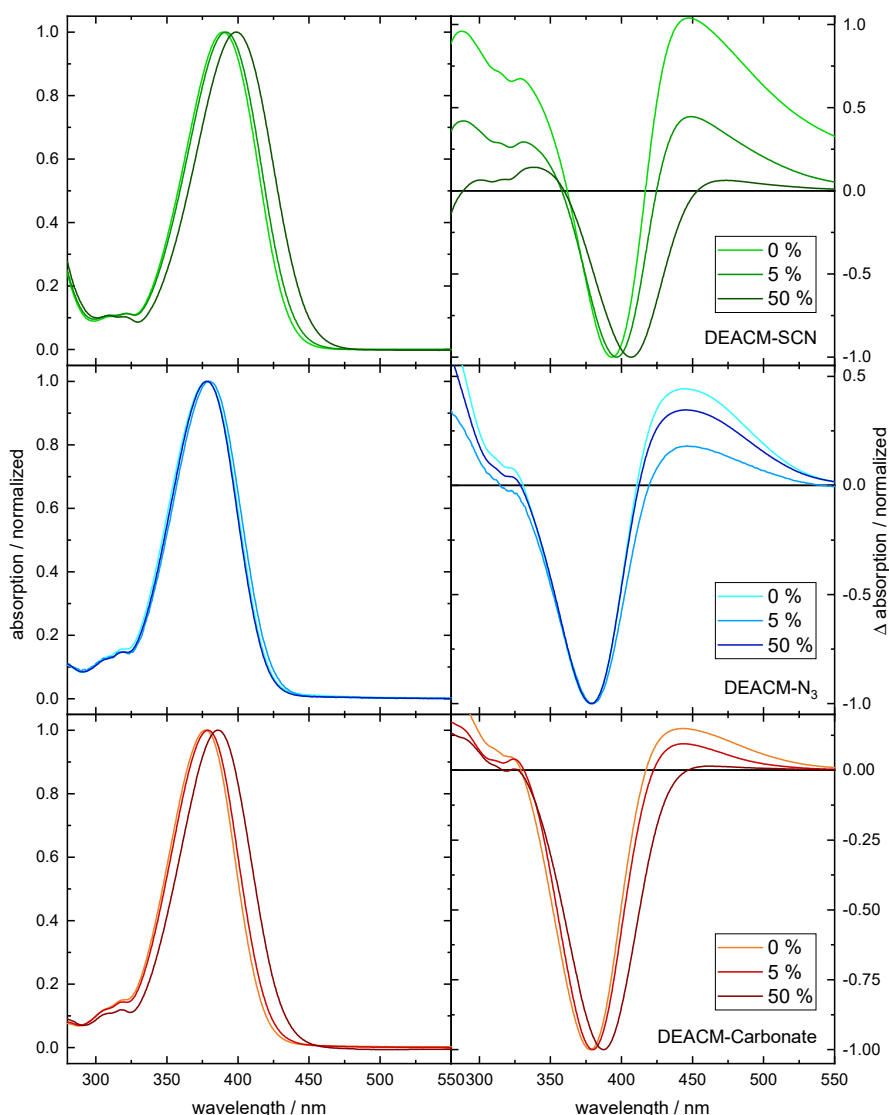


Figure S5: UV/Vis absorption spectra (left column) of DEACM-SCN (top row), DEACM-N₃ (middle row; adapted from Ref. 21 with permission from The Royal Society of Chemistry) and DEACM-Carb (bottom row). The absorption spectra are normalized to 1 and shown for all compound in pure acetonitrile and in acetonitrile/D₂O mixtures. The legend indicates the fraction of D₂O. In the right column light-minus-dark difference spectra are presented illustrating the absorption difference arising upon irradiation.

S2.2 FTIR spectra

In analogy to the UV/Vis spectra shown in Figures S4 and S5, the steady-state dark and light-induced difference spectra are measured for all compounds and all solvent mixtures and shown below in Figure S6.

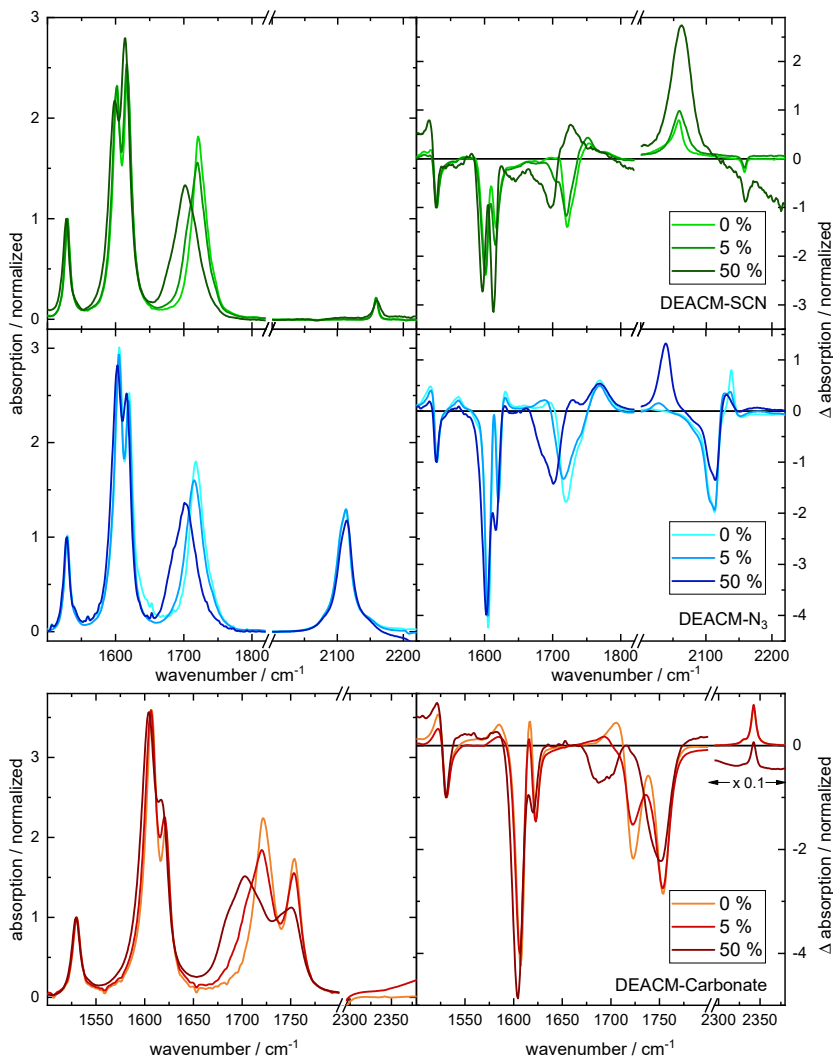


Figure S6: FTIR absorption spectra (left column) of DEACM-SCN (top row), DEACM-N₃ (middle row; adapted from Ref. 21 with permission from The Royal Society of Chemistry) and DEACM-Carb (bottom row). The absorption spectra are normalized to 1 and shown for all compound in pure acetonitrile and in acetonitrile/D₂O mixtures. The legend indicates the fraction of D₂O. In the right column light-minus-dark difference spectra are presented illustrating the absorption difference arising upon irradiation. Please note the axis break.

S3 Ultrafast pump-probe experiments

S3.1 ESA and product formation kinetics of all acetonitrile/water mixtures

Analogous to Fig. 5 of the main paper, the ESA decay and the product formation kinetics are shown and fitted with single exponentials. For DEACM-SCN the addition of water hardly influences the ESA decay, but accelerates the product formation only for 5% D₂O. See also Table S1 for an overview of the time constants. For DEACM-N₃ the ESA decay as well as the product formation become slower, while the opposite is observed for DEACM-Carb. The reason for the observed differences in kinetics is not the focus of the current study.

Table S1: Overview of time constants for all measured cages in all solvent mixtures. The time constants (in picoseconds; errors in brackets) are a result of single exponential fits to the data shown in Fig. S7

Acetonitrile/ D ₂ O vol%	ESA decay *	GSA recovery#	Product formation/ cleavage
DEACM-SCN			
100/0	11.0 (0.4)	10 (0.3)	<1 (instantaneous) 19.6 (2.1)*
95/5	15.5 (0.6)	11 (0.4)	3.8 (0.5)*
50/50	9.0 (0.6)	8.6 (0.6)	13.8 (1.7)*
DEACM-N ₃			
100/0	49.2 (0.5)	51 (2)	34 (2)*
95/5 [§]	65.4 (2.4)	78 (8)	59 (2)*
50/50	33 (3) + 140 (20)	160 (3)	44 (1)* + 320 (25)*
DEACM-Carb			
100/0	537 (5)	530 (3)	530 (3)#
95/5	543 (7)	560 (3)	560 (3)#
50/50	422 (5)	410 (3)	410 (3)#

*Resulting from fitting the curves in Fig. S7

#Resulting from global analysis

[§]Fitted with single as well as with double exponentials, the latter providing a slightly better fit

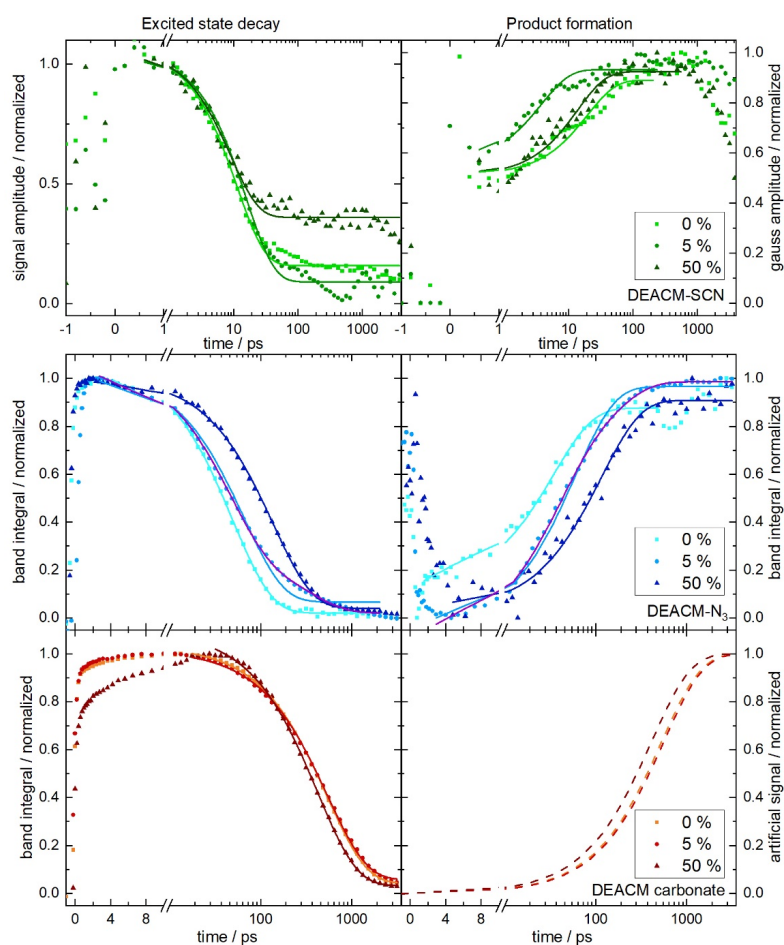


Figure S7: Traces of spectral features of DEACM-SCN (top row), DEACM-N₃ (middle row; adapted from Ref. 21 with permission from The Royal Society of Chemistry) and DEACM-Carb (bottom row) representing the reaction kinetics of the three compounds. The left column shows the decay of the excited state and the right panel shows the product formation. For DEACM-N₃ and DEACM-Carb the band integral of the CO^{a*} signal is presented to show the decay of the excited state. As this excited state is not visible for DEACM-SCN, the amplitude of the signal of the bound SCN group (maximum of ESA absorption to bleach minimum) was plotted instead. The 50% water data do not decay to zero because of a non-linear underlying broad baseline feature of water, which cannot be corrected for by a linear baseline (as is done here). To present the product formation kinetics for DEACM-SCN and DEACM-N₃ the integral of the absorption band of the free LG anion was plotted. As the ultrafast kinetics of DEACM-Carb do not show a product absorption band that can be integrated, an exponential function with the lifetime obtained from global analysis was plotted instead.

S3.2 Raw data and global analysis of 95%/5% acetonitrile/water mixture

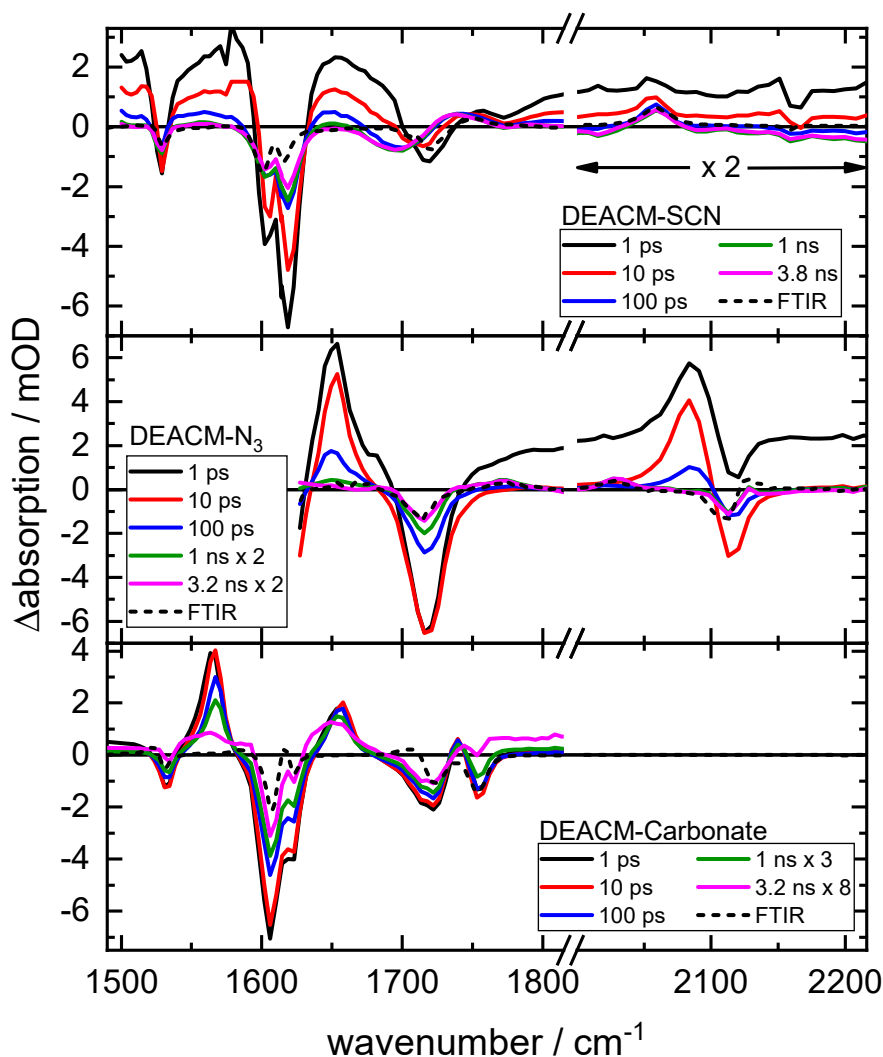


Figure S8: Ultrafast Vis-pump IR-probe data for DEACM-SCN (top panel), DEACM-N₃ (middle panel; adapted from Ref. 21 with permission from The Royal Society of Chemistry) and DEACM-Carb (bottom panel) in a mixture of 95 vol-% acetonitrile and 5 vol-% D₂O. The axes of all three plots are linked to facilitate the comparison of the different species. The time constants of the spectral cuts are given in the legend. For DEACM-SCN the data range of the SCN signal is scaled by a factor of 2. This is highlighted in the figure below the data. For the assignment of the spectral features a FTIR difference spectrum is plotted together with each species.

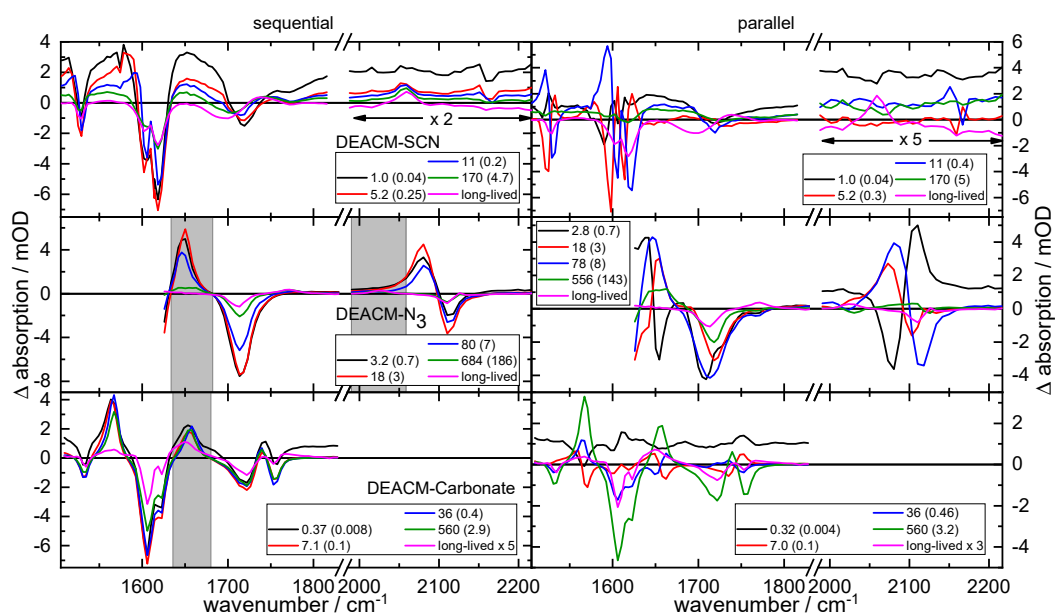


Figure S9: Spectra obtained from a global analysis of the data presented in Fig. S8. In the left panels the species associated difference spectra that are obtained by applying a sequential model to the data are shown. They feature the signals that are decaying with the lifetimes given in the legend (errors in brackets). The right panels show the decay associated difference spectra that result from applying a parallel model to the data. These spectra emphasize the differences that occur from one spectrum of the sequential model to the next. The grey bars indicate the integration limits used to determine the kinetics. The DEACM- N_3 data are adapted from Ref. 21 with permission from The Royal Society of Chemistry.

S3.3 Raw data and global analysis of 50%/50% acetonitrile/water mixture

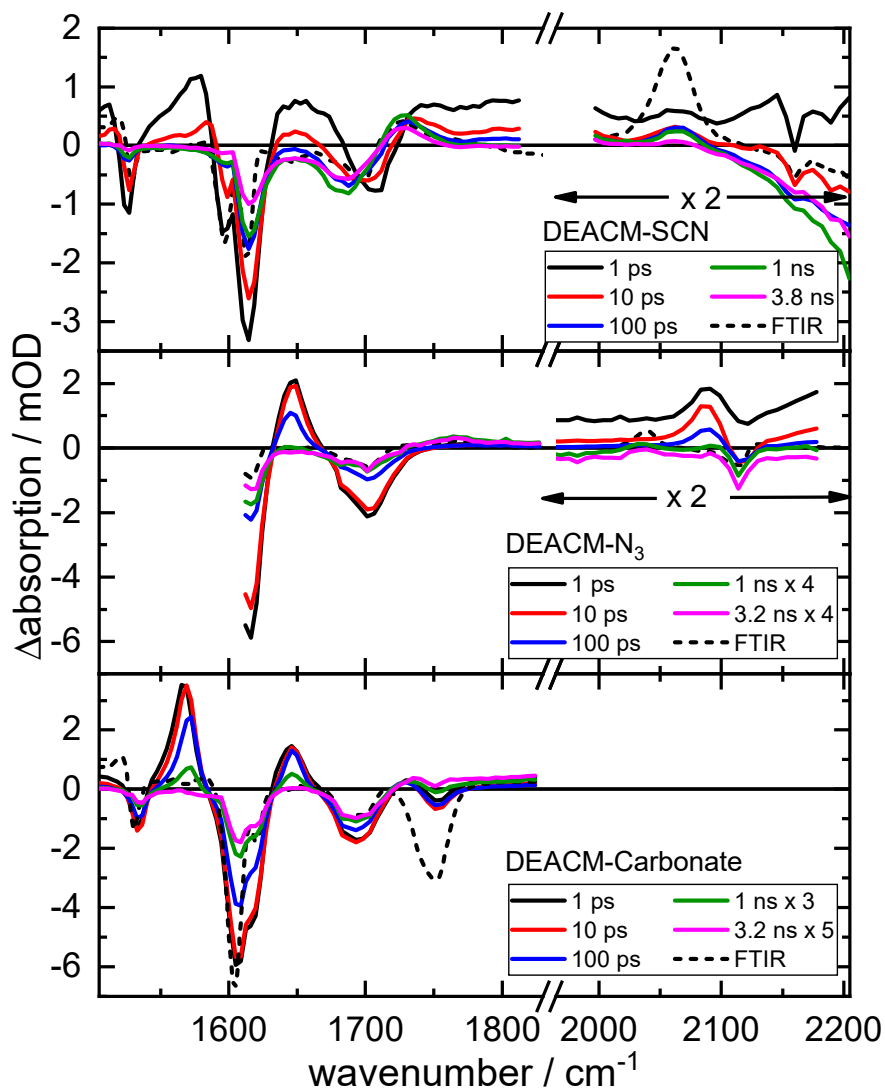


Figure S10: Ultrafast Vis-pump IR-probe data for DEACM-SCN (top panel), DEACM- N_3 (middle panel; adapted from Ref. 21 with permission from The Royal Society of Chemistry) and DEACM-Carb (bottom panel) in a mixture of 50 vol-% acetonitrile and 50 vol-% D_2O . The axes of all three plots are linked to facilitate the comparison of the different species. The time constants of the spectral cuts are given in the legend. For DEACM-SCN the data range of the SCN signal is scaled by a factor of 2. This is highlighted in the figure below the data. For the assignment of the spectral features a FTIR difference spectrum is plotted together with each species.

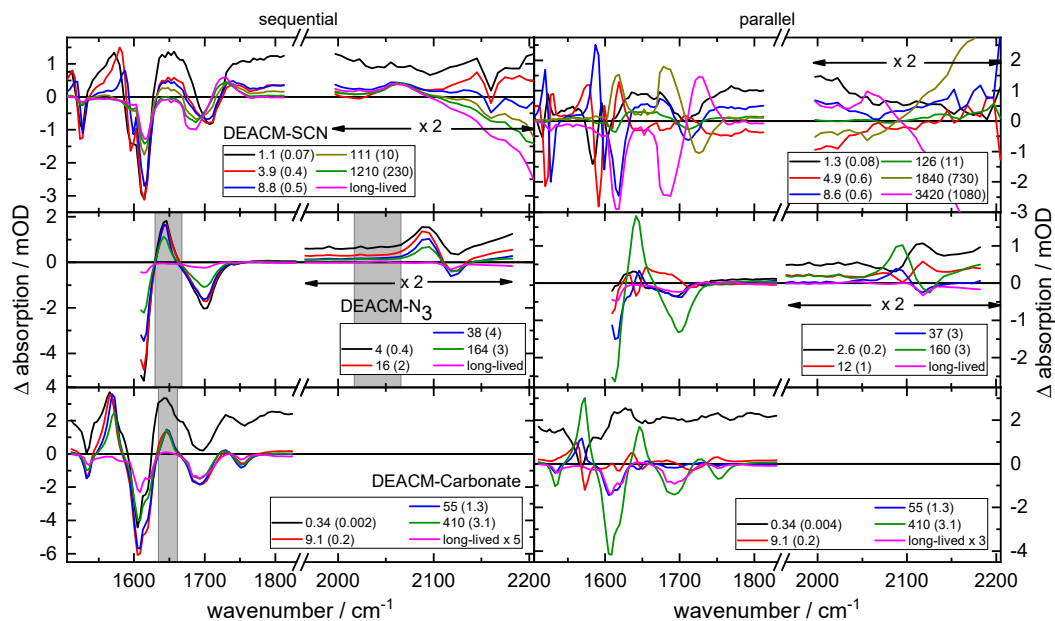


Figure S11: Spectra obtained from a global analysis of the data presented in Figure S10. In the left panels the species associated difference spectra that are obtained by applying a sequential model to the data are shown. They feature the signals that are decaying with the lifetimes given in the legend (errors in brackets). The right panels show the decay associated difference spectra that result from applying a parallel model to the data. These spectra emphasize the differences that occur from one spectrum of the sequential model to the next. The grey bars indicate the integration limits used to determine the kinetics. The DEACM- N_3 data are adapted from Ref. 21 with permission from The Royal Society of Chemistry.

S4 Computational analysis

S4.1 Optimized structures of the DEACM species

This section presents optimized ground state structures of DEACM-SCN, DEACM-N₃ and DEACM-Carb, obtained using DFT calculations at the ω B97XD / 6-31G* level of theory in vacuum. These structures were used in the excited state analysis and as reference structures in various potential energy surface scans.

Tables S2 to S4 contain the Cartesian geometries pertaining to these structures.

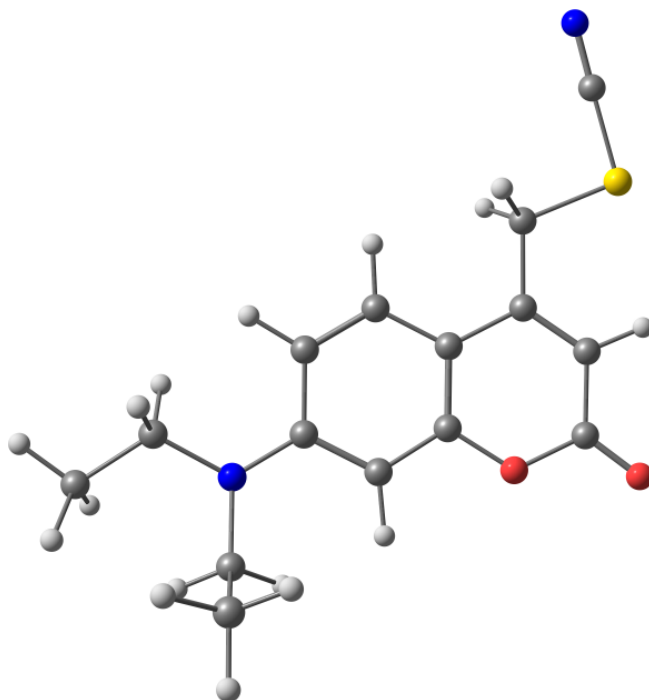


Figure S12: Optimized structure of DEACM-SCN.

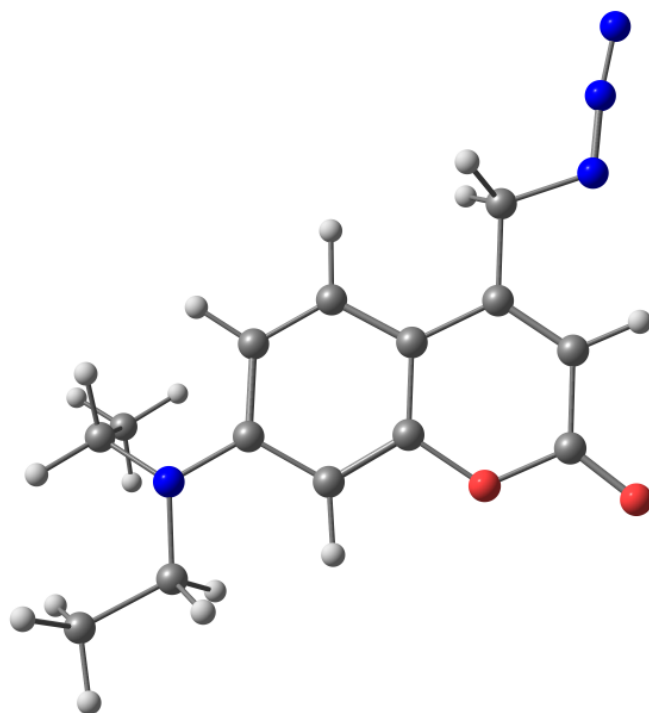


Figure S13: Optimized structure of DEACM-N₃.

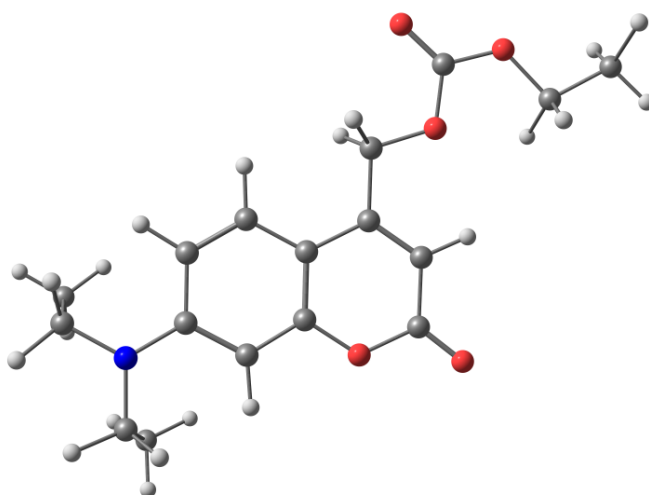


Figure S14: Optimized structure of DEACM-Carb.

Table S2: Cartesian coordinates of the ground-state optimized structure of DEACM-SCN

C	0.000000	0.000000	0.000000
C	0.000000	0.000000	1.459247
C	1.140203	0.000000	2.181001
C	2.412654	0.001903	1.486144
C	2.398088	-0.002095	0.084915
O	1.232322	-0.003245	-0.615863
C	3.556204	0.001007	-0.674762
C	4.820454	-0.004961	-0.059382
C	4.843164	0.025900	1.360492
C	3.676541	0.022025	2.094180
C	1.179405	0.002741	3.686344
S	-0.492890	-0.083834	4.444120
C	0.005776	0.010970	6.064496
N	0.346944	0.075750	7.173067
N	5.986328	-0.051354	-0.797223
C	5.934982	0.228432	-2.226929
C	5.783170	1.713375	-2.558259
O	-0.982056	0.002605	-0.695568
C	7.254866	0.138081	-0.091586
C	8.502791	-0.058315	-0.943015
H	1.664655	0.915997	4.042770
H	-0.989784	0.003790	1.901061
H	3.755151	0.043363	3.177158
H	5.779589	0.061505	1.899409
H	3.428869	0.009899	-1.748455
H	7.297088	-0.594431	0.720925
H	7.289487	1.135453	0.375271
H	9.377424	0.015206	-0.290022
H	8.516573	-1.046860	-1.412312
H	8.610235	0.703466	-1.720595
H	5.121600	-0.352127	-2.668408
H	6.842527	-0.166634	-2.684822
H	5.737949	1.862811	-3.641764
H	4.870613	2.124498	-2.115921
H	6.633317	2.285457	-2.170943
H	1.755834	-0.853891	4.045989

Table S3: Cartesian coordinates of the ground-state optimized structure of DEACM-N₃

N	-6.183588	-2.465985	0.052744
C	-3.158405	-1.137030	-0.080127
H	-2.911052	-1.750430	0.798332
C	-2.272003	0.079445	-0.095007
C	-0.837686	-0.118837	-0.135429
C	-2.768908	1.332071	-0.075186
C	-0.182887	-1.358122	-0.146446
C	-0.019324	1.018025	-0.154853
H	-3.832981	1.526781	-0.045689
C	1.192036	-1.461010	-0.183081
H	-0.762417	-2.276492	-0.118122
C	1.364227	0.940858	-0.192805
C	2.014365	-0.304840	-0.225828
H	1.627812	-2.450323	-0.169956
H	1.899539	1.880297	-0.194912
O	-0.543559	2.271883	-0.131351
C	-1.904989	2.506286	-0.088903
O	-2.275554	3.651414	-0.067322
N	3.391993	-0.403757	-0.310175
C	3.993948	-1.726286	-0.139673
C	5.499659	-1.783423	-0.366218
H	3.531800	-2.400245	-0.868357
H	3.763615	-2.130052	0.859604
H	5.815418	-2.829515	-0.311179
H	5.770112	-1.402849	-1.356041
H	6.064737	-1.231433	0.390478
C	4.204760	0.771153	-0.021658
C	4.301522	1.104616	1.467553
H	3.806319	1.619335	-0.583112
H	5.200974	0.606099	-0.433866
H	4.903882	2.005564	1.622108
H	3.309944	1.276590	1.897192
H	4.770376	0.282164	2.018954
H	-2.948107	-1.745066	-0.971589
N	-4.570476	-0.743554	-0.050350
N	-5.362616	-1.684364	0.002838

Table S4: Cartesian coordinates of the ground-state optimized structure of DEACM-Carb

O	0.653862	2.332111	0.103504
C	1.149415	1.068659	0.181018
C	0.306758	-0.050082	0.176476
C	-1.119193	0.176546	0.088283
C	-1.587443	1.439629	0.014437
C	-0.700047	2.594037	0.018058
C	2.529978	0.963071	0.257093
C	3.147017	-0.296665	0.345424
C	2.299463	-1.436722	0.329101
C	0.930626	-1.305256	0.251753
C	-2.027501	-1.018879	0.083166
O	-3.377812	-0.584294	-0.002426
C	-4.291171	-1.574227	-0.025133
O	-4.030308	-2.747237	0.020058
O	-1.045871	3.746131	-0.046982
O	-5.531970	-1.106798	-0.104156
C	-5.768948	0.311527	-0.152970
C	-7.267776	0.505175	-0.234840
H	-2.643953	1.660710	-0.051826
H	0.328371	-2.209291	0.247187
H	2.715431	-2.434343	0.379073
N	4.512799	-0.421113	0.463584
H	3.091784	1.887103	0.240598
H	-1.892562	-1.611363	0.994972
H	-1.800833	-1.673573	-0.765690
H	-5.261185	0.732088	-1.026221
H	-5.351909	0.777868	0.744690
H	-7.670584	0.028148	-1.132386
H	-7.498601	1.574021	-0.273987
H	-7.761427	0.073429	0.639968
C	5.370121	0.754799	0.419491
C	5.150600	-1.729058	0.414446
C	5.237637	-2.343499	-0.984699
C	5.624014	1.306497	-0.985425
H	4.939735	1.531211	1.061051
H	6.322368	0.480611	0.883522
H	6.157659	-1.612332	0.825254
H	4.629915	-2.410242	1.096742
H	6.217917	2.224805	-0.930349
H	6.172538	0.583750	-1.596706
H	4.684634	1.536615	-1.496728
H	5.682583	-3.342824	-0.932863
H	4.247295	-2.432535	-1.441143
H	5.856720	-1.728687	-1.644308

S4.2 Ground-state equilibrium structures: dihedral angle α_{CCCX}

The ground state equilibrium structure of the different DEACM species varies considerably with respect to the dihedral angle α_{CCCX} . In the case of DEACM-SCN, the global minimum corresponds to a twisted structure, with $\alpha_{\text{CCCS}} = 103^\circ$, while a local linear minimum is found at $\alpha_{\text{CCCS}} = 3^\circ$ (see Fig. S15). In contrast to this, in the cases of DEACM-N₃ and CEACM-Carb, the global minimum structure is linear, and a local minimum exists at the twisted geometry (see Figs. S16 and S17). DFT calculations were again performed at the $\omega\text{B97XD} / 6\text{-31G}^*$ level of theory. Other DFT functionals (PBE0, BHandHLYP) yield very similar results.

Table S5 indicates the energy differences between the twisted vs. linear structures, along with the barrier heights obtained from the relaxed surface scans shown in Figs. S15-S17. For comparison, data in vacuum and in a solvent environment (acetonitrile and water) are shown; clearly, the results do not differ significantly.

Table S5: Ground-state energy differences between the linear and the twisted geometries for the DEACM-SCN, DEACM-N₃, and DEACM-Carb systems, in vacuum as well as acetonitrile and water, treated at the Polarizable Continuum Model (PCM) level. Note that for DEACM-SCN the twisted structure is more stable, whereas in the other cases the linear structure is energetically favored. The ground-state barrier heights as well as the populations (Boltzmann weights at room temperature) of both states are also given in this table. Barrier heights were reported in such a way that the larger barriers were reported in all cases (i.e., linear \rightarrow twisted for DEACM-SCN and twisted \rightarrow linear for the other systems.)

System	environment	ΔE [eV] (linear – twisted)	ΔE [eV] (barrier)	P_{thermal} [%] (linear)	P_{thermal} [%] (twisted)
DEACM-SCN	vacuum	−0.0790	0.1006	4	96
	acetonitrile	−0.0753	0.0921	5	95
	water	−0.0753	0.0918	5	95
DEACM-N ₃	vacuum	0.0237	0.1373	71	29
	acetonitrile	0.0260	0.1231	73	27
	water	0.0259	0.1227	73	27
DEACM-Carb	vacuum	0.0102	0.1364	60	40
	acetonitrile	0.0187	0.1205	67	33
	water	0.0187	0.1199	67	33

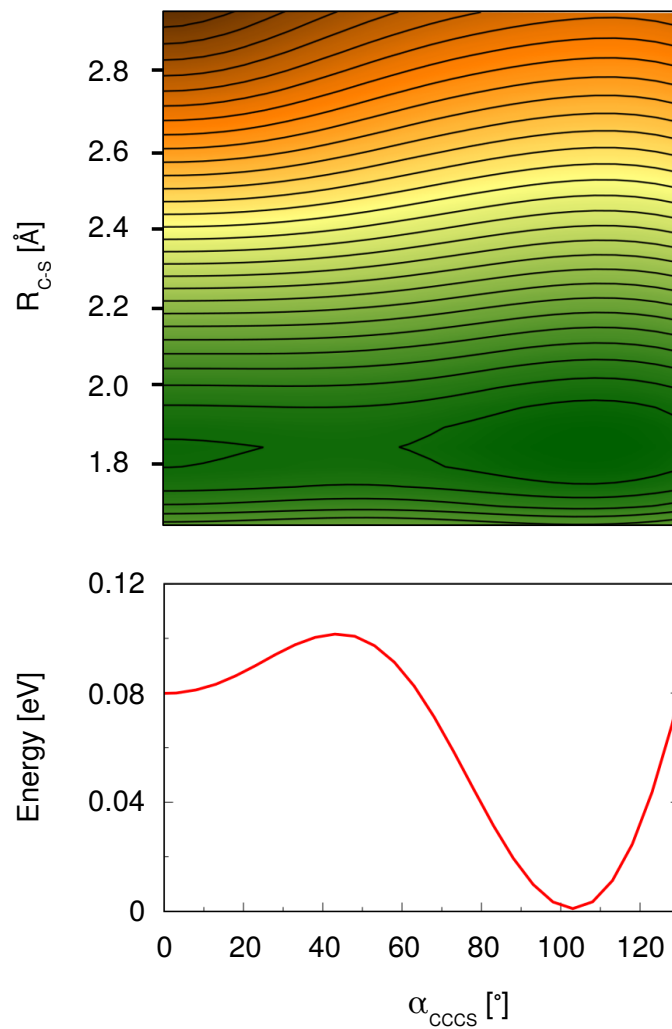


Figure S15: In the upper panel, a two-dimensional PES of the S₀ state along the C-S bond distance and the CCCS dihedral angle is shown, for the DEACM-SCN species in vacuum. The lower panel shows a one-dimensional relaxed scan of the S₀ PES at a R_{C-S} equilibrium distance of 1.838 Å.

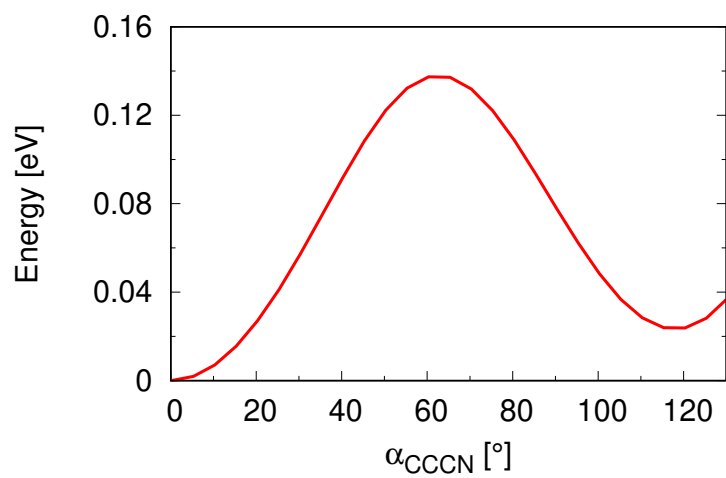


Figure S16: One-dimensional relaxed scan of the S₀ PES for the DEACM-N₃ species at the R_{C-N}=1.466 equilibrium distance in vacuum.

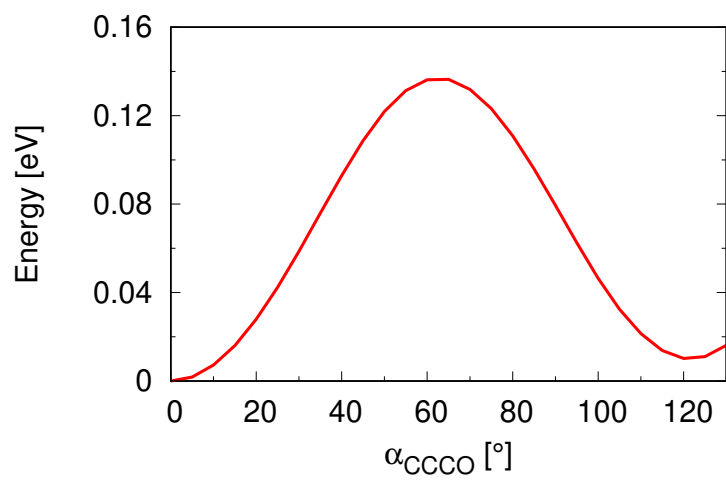


Figure S17: One-dimensional relaxed scan of the S₀ PES for the DEACM-Carb species at the R_{C-O}=1.421 equilibrium distance in vacuum.

S4.3 Constraints for relaxed surface scans

Due to the complex nature of relaxed surface scans, several geometric constraints had to be imposed on the degrees of freedom of the leaving groups during these calculations, to ensure numerical stability. In DEACM- N_3 , the azide bending angle α_{NNN} and the dihedral angle α_{NNCC} that corresponds to a rotation of the whole azide group were kept fixed (see Fig. S18). An equivalent set of coordinates were constrained in the case of DEACM-SCN. Since the carbonate leaving group has a higher conformational flexibility, a total of two angles and one dihedral angle had to be constrained to prevent unphysical bonding effects with the coumarin framework, especially at longer C-O bond lengths (see Fig. S19).

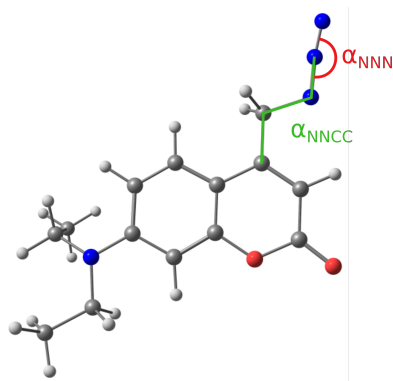


Figure S18: The angle α_{NNN} and the dihedral angle α_{NNCC} that were kept fixed at their respective initial values during the relaxed surface scan of DEACM- N_3 .

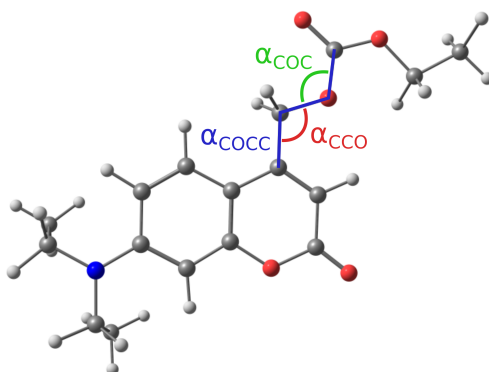


Figure S19: The α_{CCO} and α_{COC} angles as well as the dihedral angle α_{COCC} that were kept fixed at their respective initial values during the relaxed surface scan of DEACM-Carb.

S4.4 Vertical excitations

Vertical excitations were analyzed for singlet and triplet states, with energies up to the S_3 state, for DEACM-SCN, DEACM- N_3 and DEACM-Carb. All TDDFT calculations were performed at the ω B97XD / 6-31G* level of theory.

Table S6: Vertical excitation energies and oscillator strengths (f) of DEACM-SCN in vacuum.

state	excitation energy [eV]	f
S_3	4.9991	0.0001
T_7	4.8398	0.0000
S_2	4.7955	0.0327
T_6	4.5799	0.0000
T_5	4.5684	0.0000
T_4	4.3840	0.0000
S_1	4.1472	0.4779
T_3	4.1116	0.0000
T_2	3.8066	0.0000
T_1	2.7115	0.0000

Table S7: Vertical excitation energies and oscillator strengths (f) of DEACM- N_3 in vacuum.

state	excitation energy [eV]	f
S_3	4.8342	0.0487
T_8	4.6339	0.0000
T_7	4.5750	0.0000
S_2	4.4680	0.0001
T_6	4.4007	0.0000
S_1	4.2167	0.4728
T_5	4.1417	0.0000
T_4	4.1085	0.0000
T_3	3.9245	0.0000
T_2	3.8131	0.0000
T_1	2.7361	0.0000

Table S8: Excited State Energies and Oscillator strength of DEACM-Carb in vacuum.

State	Energy [eV]	Oscillator strength
S ₃	5.0405	0.0001
S ₂	4.7986	0.0434
T ₆	4.6274	0.0000
T ₅	4.6098	0.0000
T ₄	4.3923	0.0000
S ₁	4.1836	0.4880
T ₃	4.0716	0.0000
T ₂	3.8310	0.0000
T ₁	2.7265	0.0000

S4.5 Geometry optimization in the S_1 state

All 1D and 2D “relaxed scans” reported in the manuscript were performed with partial optimization in the ground state followed by single-point excited-state calculations, as explained in Sec. 3. This approach was motivated by the fact that several excited states may be involved in the photochemistry, and ground-state optimization for a reduced-dimensional (R_{C-X}, θ) 2D cut would provide a reasonable approximation. The key assumption here is that (i) the two “reaction coordinates” (R_{C-X}, θ) play a dominant role in the photochemistry, and (ii) the reorganization of the other coordinates is of secondary importance and can be reasonably approximated by the ground-state optimization. However, given that the S_1 state is found to play a dominant role, S_1 optimization could be a better alternative (even though care should be taken regarding the involvement of higher excited states). Obviously, the present level of analysis cannot provide a full picture of the excited-state dynamics.

To assess the role of vibrational reorganization in the S_1 state, we carried out excited-state optimization as illustrated in Figs. S20-S21 below. For DEACM-SCN, both 1D and 2D PES cuts are shown. In these illustrations, PES cuts based on S_0 optimization (l.h.s.) are compared with S_1 optimization (r.h.s.). The 1D PES cut (Fig. S20) shows, as expected, that the S_1 state is stabilized under state-specific optimization, while the energetics of the other states is modified. The 2D PES cut of S_1 (Fig. S21) confirms an overall stabilization – especially at smaller distances – and, importantly, shows that the overall PES topology is not strongly modified.

In the case of the other DEACM-LG systems, however, S_1 optimization led to artifacts, due to state mixing at the geometries of the S_1/S_2 crossings.

Apart from technical issues, we conclude that the chosen approach – i.e., geometry optimization in the ground state combined with an (R_{C-X}, θ) scan by TDDFT – is acceptable, even though the energetics would be modified to some extent if excited-state optimization was carried out (see the above results for DEACM-SCN). Given that the excited-state processes involve the participation of several electronic states due to nonadiabatic effects, a more demanding dynamical and/or kinetic treatment would be necessary to obtain a reliable theoretical estimate of dissociation time scales and quantum yields.

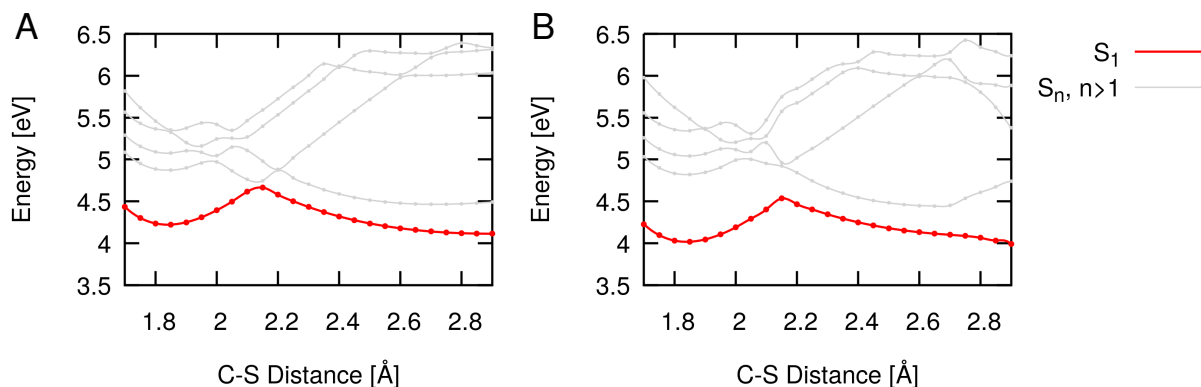


Figure S20: 1D PES scans for DEACM-SCN as a function of R_{C-X} , with $\theta = 0$: (A) same conditions as shown in Fig. 9 of the manuscript, with partial ground-state optimization, and (B) using geometry optimization in the S_1 state. It is seen that in the latter case, the S_1 state is stabilized, and the barrier increases by 0.06 eV. Also, the energetics of the higher-lying singlet states is shifted.

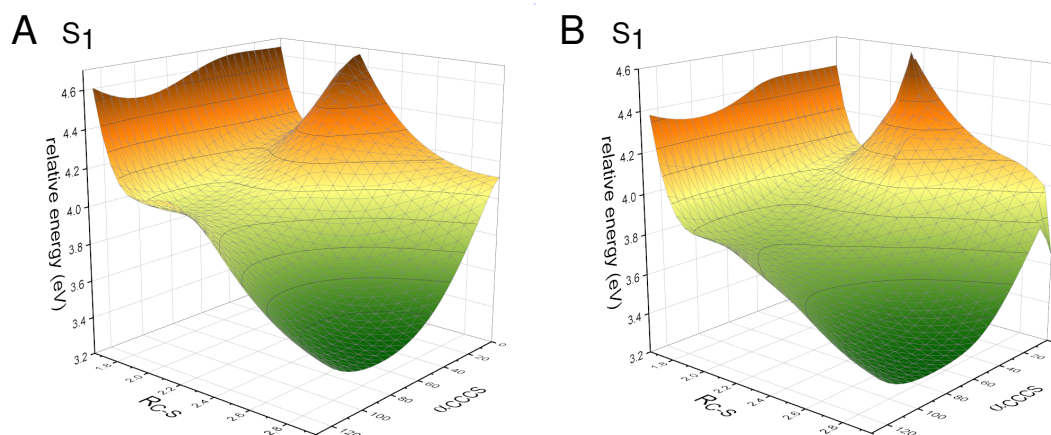


Figure S21: 2D S_1 PES scans for DEACM-SCN as a function of (R_{C-X}, θ) : (A) using partial ground-state optimization, (B) using geometry optimization in the S_1 state. It is seen that in B, the S_1 state is significantly stabilized at smaller distances, but the overall topology of the 2D PES remains largely unchanged.

S4.6 Solvent effects on excited states

Analysis of solvent effects on the excited state calculations of singlet states up to the S_5 state was carried out for DEACM-SCN, DEACM- N_3 and DEACM-Carb using the Linear-Response Polarizable Continuum Model (LR-PCM) in the non-equilibrium regime (i.e., standard option in Gaussian for excitation energies). In all cases, acetonitrile has been considered to match the experiments reported in the present paper, and we also compared with water. All TDDFT calculations were performed at the ω B97XD / 6-31G* level of theory.

As can be seen from these data, solvent effects at the LR-PCM level are not pronounced at the Franck-Condon geometry, of the order of 0.2 eV at most. Also, acetonitrile and water yield very similar effects.

Table S9: Solvent effects on the vertical excitation energies and oscillator strengths (f) of DEACM-SCN, as compared with reference calculations in vacuum.

state	excitation energy [eV]	f
vacuum		
S_5	5.2920	0.0001
S_4	5.2743	0.0344
S_3	4.9991	0.0001
S_2	4.7955	0.0327
S_1	4.1472	0.4779
acetonitrile		
S_5	5.3136	0.0003
S_4	5.2956	0.0001
S_3	5.2118	0.0607
S_2	4.7493	0.0249
S_1	3.9752	0.5833
water		
S_5	5.3215	0.0003
S_4	5.2959	0.0001
S_3	5.2125	0.0608
S_2	4.7489	0.0247
S_1	3.9750	0.5809

Table S10: Solvent effects on the vertical excitation energies and oscillator strengths (f) of DEACM-N₃, as compared with reference calculations in vacuum.

state	excitation energy [eV]	f
vacuum		
S ₅	5.3318	0.0317
S ₄	5.0097	0.0001
S ₃	4.8342	0.0487
S ₂	4.4680	0.0001
S ₁	4.2167	0.4728
acetonitrile		
S ₅	5.3386	0.0004
S ₄	5.2644	0.0563
S ₃	4.7786	0.0363
S ₂	4.4557	0.0002
S ₁	4.0411	0.5860
water		
S ₅	5.3469	0.0003
S ₄	5.2647	0.0565
S ₃	4.7779	0.0359
S ₂	4.4558	0.0002
S ₁	4.0404	0.5836

Table S11: Solvent effects on the vertical excitation energies and oscillator strengths (f) of DEACM-Carb as compared with reference calculations in vacuum.

state	excitation energy [eV]	f
vacuum		
S ₅	5.9949	0.1656
S ₄	5.3272	0.0252
S ₃	5.0405	0.0001
S ₂	4.7986	0.0434
S ₁	4.1836	0.4880
acetonitrile		
S ₅	5.8276	0.2677
S ₄	5.3355	0.0002
S ₃	5.2514	0.0451
S ₂	4.7426	0.0372
S ₁	3.9988	0.5957
water		
S ₅	5.8259	0.2667
S ₄	5.3426	0.0002
S ₃	5.2516	0.0452
S ₂	4.7419	0.0370
S ₁	3.9982	0.5932

S4.7 Effect of LR-PCM vs. state-specific (SS-PCM) solvation

While the LR-PCM model is suitable for the single-point excited-state calculations reported in Sec. S9 of the ESI, its use for geometries away from the Franck-Condon region, along the photochemical path in the (R_{C-X}, θ) space – including the calculations for the transition states reported in Table 6 – is more approximate. The non-equilibrium regime that was employed (which corresponds to the standard option in the Gaussian package to compute vertical excitations), is physically correct for the vertical excitation energies reported in Tables S9-S11, but does not include state-specific solvent relaxation effects. In the following, we briefly characterize the results obtained with LR-PCM for 2D PES scans and comment on a comparison with the state-specific (SS)-PCM model.

In Fig. S22, we report the effect of LR-PCM solvation on the 2D PES scans in the various DEACM-LG systems, analogously to Fig. 10 of the manuscript. In these calculations, the evolution of the PCM cavity was monitored and found to systematically increase with the R_{C-X} distance, but decrease with an increasing value of the dihedral twist θ coordinate. The 2D barrier heights reported in Table 6 (column “2D(PCM)”) of the main manuscript text refer to the transition states obtained from the 2D PESs for acetonitrile. As reported in the manuscript, the reaction in DEACM-SCN remains barrierless, while the barrier increases in DEACM- N_3 as compared with the vacuum case due to a stabilization in the reactant region. In DEACM-Carb, however, the barrier height is reduced as compared with the vacuum case.

To estimate the energetic effects of excited-state solvent equilibration, we conducted additional calculations, where the state-specific (SS)-PCM model was used for the S_1 and S_2 states of DEACM- N_3 whose crossing is dominant in defining the S_1 barrier. These calculations, shown in Fig. S23, suggest that, while the general picture remains unchanged, the S_1 state is typically stabilized by ~ 0.2 eV in acetonitrile or water as compared with LR-PCM, and the S_1 barrier tends to increase slightly more because the position of the barrier is modified. (Indeed, the S_2 state seems to be less sensitive to state-specific solvation such that the S_1 - S_2 gap increases, entailing a shift in the transition state).

For the other DEACM-LG systems, it proved unfeasible to obtain reliable results since various state crossings occur that are found to induce discontinuities in the SS-PCM calculations.

Overall, the LR-PCM method is technically preferable in the present study since it gives a partial description of solvation effects while producing smooth PESs (as shown in Fig. S22). However, the method generally underestimates the solvent-induced state-specific stabilization. A more refined study would introduce state-specific dynamic solvation in the subset of nonadiabatically coupled states that are relevant for the excited-state dynamics.

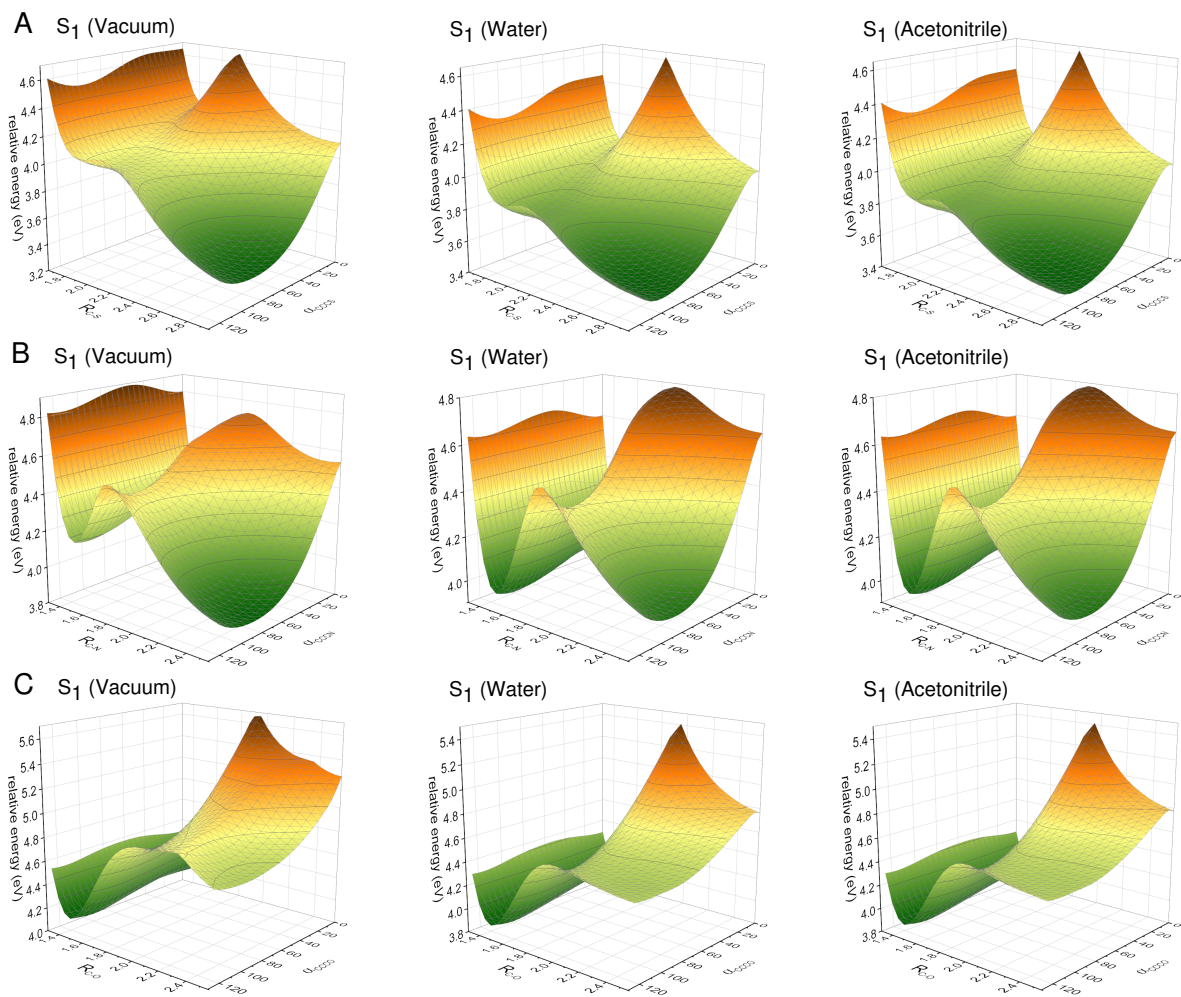


Figure S22: 2D scans using the LR-PCM solvation model for (A) DEACM-SCM, (B) DEACM-N₃, and (C) DEACM-Carb, in acetonitrile and water, as compared with the vacuum case.

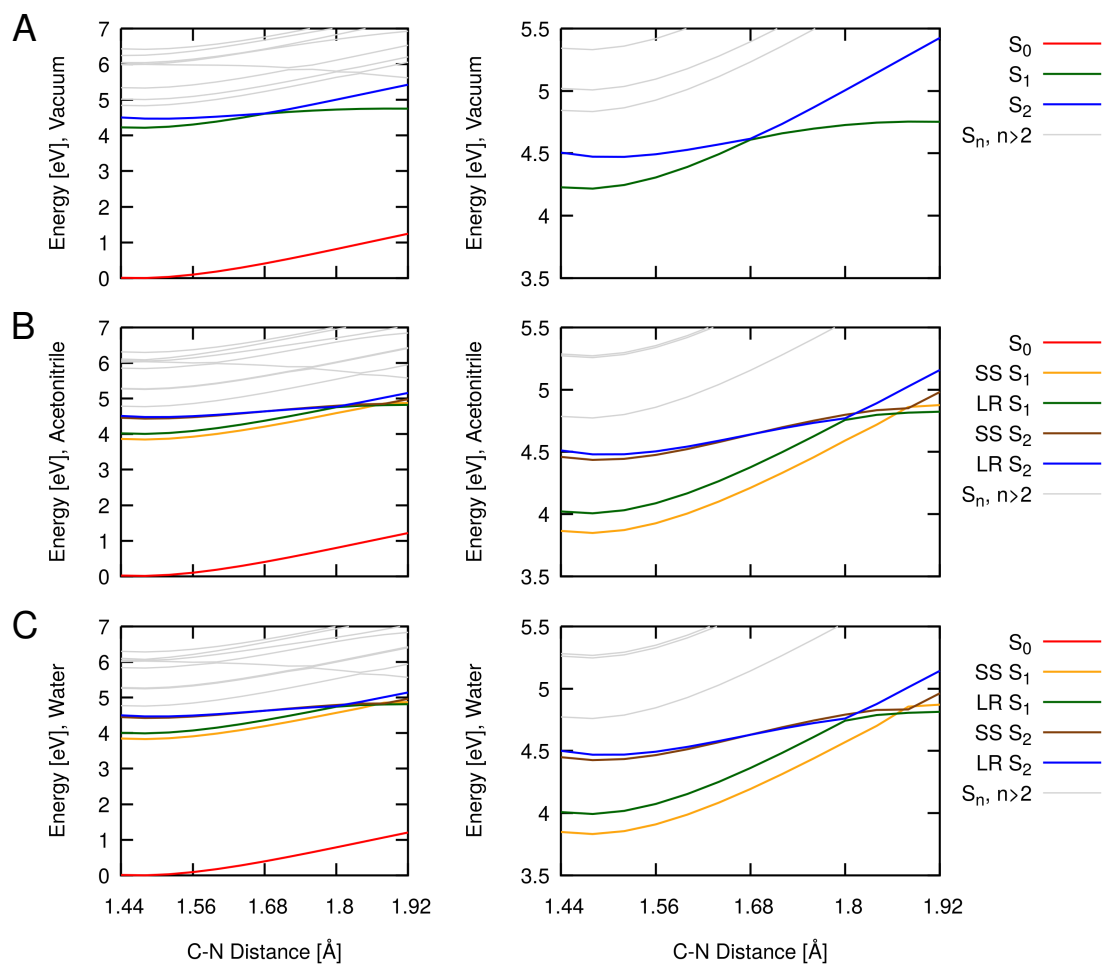


Figure S23: Solvent-specific (SS)-PCM calculations for the S_1 and S_2 states of the DEACM- N_3 system (labelled “SS”), as compared with the Linear Response (LR)-PCM calculations (labelled “LR”) that were employed to compute the barrier heights reported in Table 6 of the manuscript. All l.h.s. panels refer to an energy range of 0-7 eV whereas all r.h.s. panels show the same data in an energy range of 3.5-5.5 eV. (A) Vacuum calculations, for reference, (B) PCM/acetonitrile calculations, (C) PCM/water calculations. The S_1 state is found to be stabilized to a similar extent in acetonitrile and water.

S4.8 Charge analysis as a function of R_{C-X} distance

To obtain some insight into how the excited-state charge distribution evolves along the R_{C-X} distance coordinate, we computed partial charges of the leaving group (LG) fragment for the adiabatic S_1 state of the DEACM-SCN, DEACM- N_3 and DEACM-Carb systems. These partial charges as a function of R_{C-X} are shown in Figs. S24-S26, along with the one-dimensional PES cuts for these systems. Charges were calculated using the Natural Bond Orbital (NBO) analysis and the Mulliken charge analysis. Both methods yield very similar results. TDDFT calculations were performed at the ω B97XD / 6-31G* level of theory.

In the lower panels of the figures, vertical dashed lines indicate the positions of the curve crossings that lead to a sudden change in charge character of the S_1 state. While these sudden changes do not convey a realistic picture of the LG dissociation pathway — which is going to feature a smooth change in charge distributions, and will involve superpositions of adiabatic states, rather than exclusively the S_1 state which is shown here — one can infer an overall trend which shows that the dissociative S_1 state accumulates negative charge on the LG moiety as expected. As can be seen from the figures, the details of the charge evolution differ between the three systems, but the overall picture is similar in that the crossing with dissociative states induces progressive polarization of the lowest singlet state(s) in the dissociation limit.

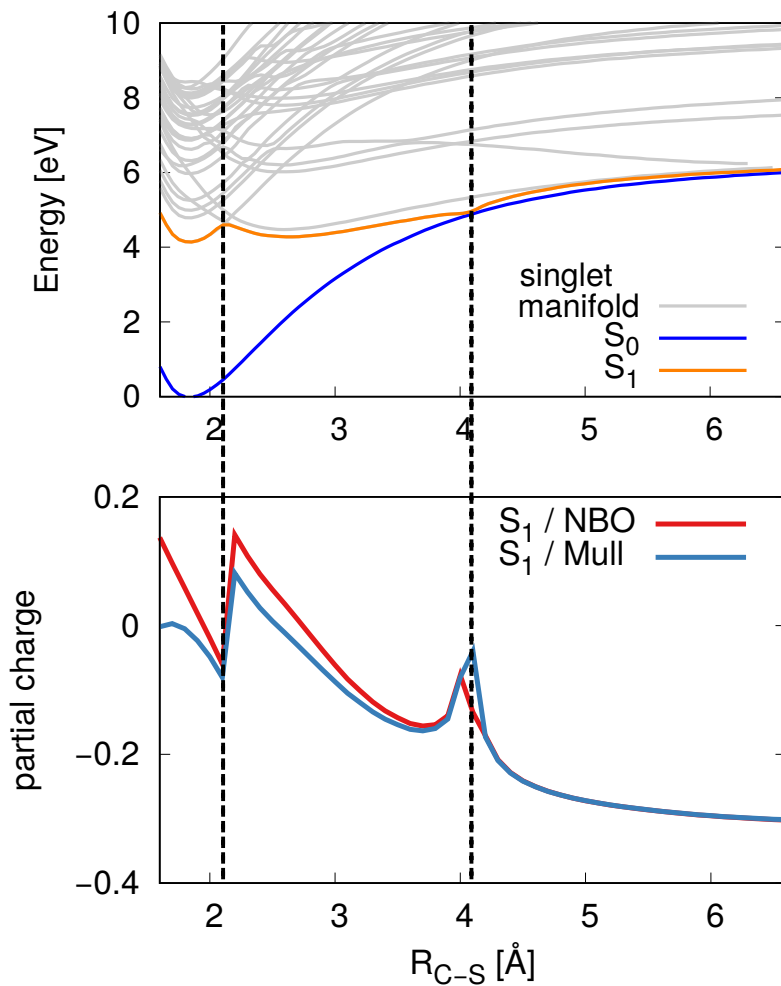


Figure S24: Upper panel: For DEACM-SCN, adiabatic singlet PESs are shown, analogously to Fig. 8 and Fig. 9 of the main text. Lower panel: Partial charges of the SCN fragment in the S_1 state as a function of the R_{C-X} coordinate. As explained above, the vertical dashed lines indicate the positions of the curve crossings that lead to a sudden change in charge character of the S_1 state.

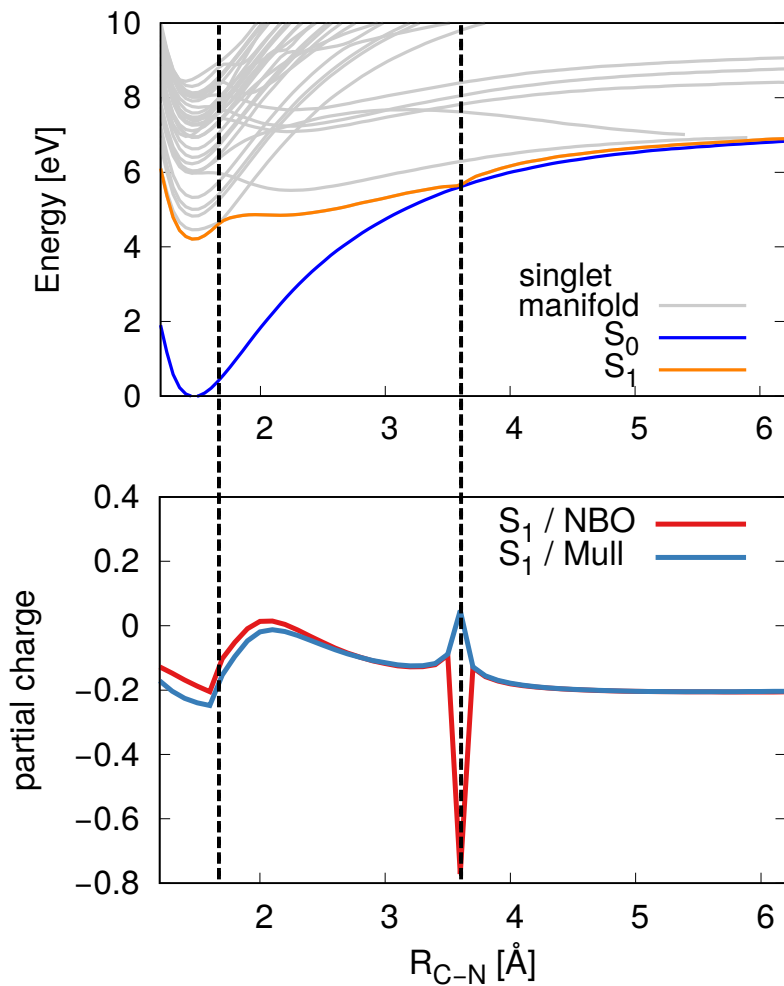


Figure S25: Upper panel: For DEACM- N_3 , adiabatic singlet PESs are shown, analogously to Fig. 8 and Fig. 9 of the main text. Lower panel: Partial charges of the N_3 fragment in the S_1 state as a function of the DEACM- N_3 dissociation coordinate. Vertical dashed lines again indicate state crossings that induce a change in S_1 charge character.

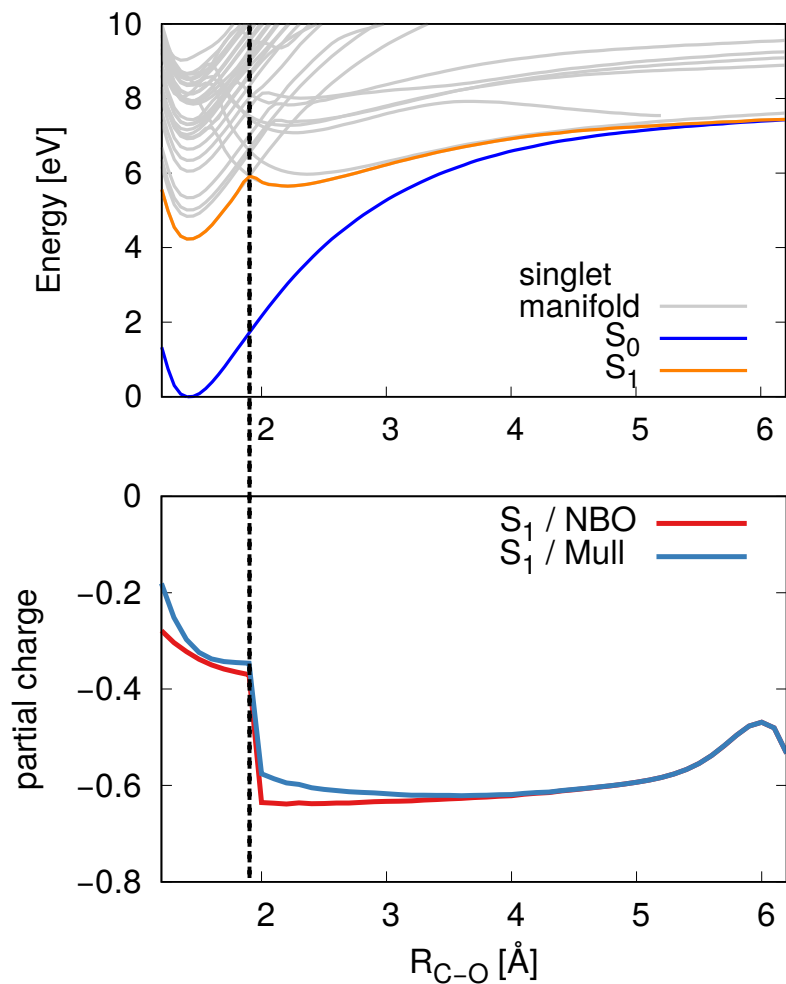


Figure S26: Upper panel: For DEACM-Carb, adiabatic singlet PESs are shown, analogously to Fig. 8 and Fig. 9 of the main text. Lower panel: Partial charges of the Carb fragment in the S_1 state as a function of the DEACM-Carb dissociation coordinate. Vertical dashed lines again indicate state crossings that induce a change in S_1 charge character.

S4.9 State crossings of low-lying singlet states with dissociative states

As can be inferred from Fig. 9 of the main text, all DEACM-LG systems under investigation exhibit state crossings of the S_1 and S_2 states (along with crossings of the S_1 states with other S_n states at larger distances) which lead to a change in electronic character, inducing dissociative behavior of the S_1 state. More detailed inspection of Fig. 9 shows that multiple sequences of such state crossings occur, involving the stabilization of dissociative states that correspond to higher excitations at the Franck-Condon geometry. To illustrate this, Fig. S27 highlights that such “diabatic” dissociative states (dashed lines) descend in energy, as a function of R_{C-X} , and undergo a series of curve crossings that finally lend dissociative character to the S_1 state. The figure is based on the same data as Fig. 9 of the main text.

To obtain Fig. S27, we did not carry out any diabaticization procedure in a rigorous sense, and for this reason used the term “diabatic” in quotation marks. However, it is clear by inspection of the PES cuts that many successive crossings occur, entailing a change of state character. If one takes each of these crossings as an isolated two-state system, one would infer from the weakly avoided character of the crossing that the resulting diabatic couplings are small, and the diabatic and adiabatic states coincide as soon as one moves away from the crossing region. For a number of such crossings, we analyzed the orbital transitions in detail, confirming that intuitive continuation of the potential surfaces across each two-state intersection leads to conservation of the state character – as expected for diabatic states. Further, as reported in Sec. S11 and Figs. S20-S22, we analyzed the change in electronic character of the S_1 state by Natural Bond Order (NBO) analysis and Mulliken charge analysis.

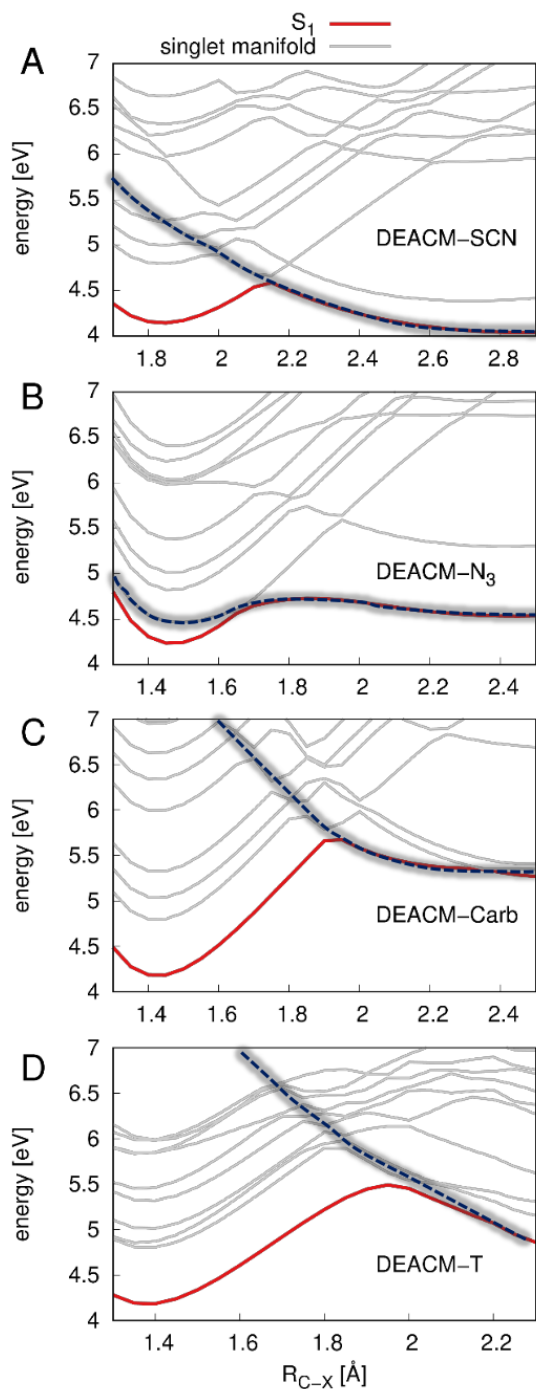


Figure S27: Complementary to Fig. 9 of the main text, the figure illustrates the evolution of the singlet manifold in the various DEACM-LG systems as a function of the R_{C-X} coordinate. In addition to the adiabatic states shown in Fig. 9 of the main text, the present figure indicates “diabatic” dissociative states (dashed lines) whose character is adopted by the S_1 state beyond the S_1-S_2 crossing point (or S_1-S_n crossing points at larger R_{C-X}). These diabatic states can be followed by inspection through a series of avoided crossings.